



Photocatalytic conversion of CO₂ to acetic acid by CuPt/WO₃: Chloride enhanced C-C coupling mechanism

Di Zeng^a, Haipeng Wang^a, Xiaodi Zhu^c, Heng Cao^c, Wenjing Wang^a, Yu Zhang^a, Juxue Wang^a, Ling Zhang^{a,*}, Wenzhong Wang^{a,b,**}

^a State Key Laboratory of High Performance Ceramics and Superfine Microstructure, Shanghai Institute of Ceramics Chinese Academy of Sciences, Shanghai 200050, China

^b School of Chemistry and Materials Science, Hangzhou Institute for Advanced Study, University of Chinese Academy of Sciences, Hangzhou 310024, China

^c National Synchrotron Radiation Laboratory, University of Science and Technology of China, Hefei, Anhui 230029, China

ARTICLE INFO

Keywords:

Photocatalytic CO₂ reduction
CH₃COOH
C-C coupling
Chloride coordination
Single-atom Cu

ABSTRACT

Photocatalytic converting CO₂ into value-added C₂₊ fuels has attracted intense attention for CO₂ capture and utilization. Cu-based catalysts have shown the potential of photocatalytic CO₂ reduction for multi-carbon (C₂₊) production. However, how the valance state and coordination environment affect the C-C coupling mechanism is unclear and requires further investigation. Herein, we investigate the influence of the coordination environments of hexagonal tungsten oxide (WO₃) photocatalyst loading with single-atom Cu and Pt. In this system, Cu(I) is stabilized by forming a coordinated complex, which increased the adsorption capacity of CO and extended the lifetime of CO* intermediate. Simultaneously, adjacent Pt sites provided protons for the hydrogenation of CO* intermediate. The results demonstrated that the coordination of chlorine ions with Cu/Pt was beneficial to the formation of C₂₊ products. In this work, the Cu2Pt2/WO₃ exhibits a high photocatalytic CO₂ reduction activity with a yield of 19.41 μmol g⁻¹ h⁻¹ and a selectivity of 88.1%.

1. Introduction

Converting greenhouse gas CO₂ into value-added chemicals is a crucial step towards a sustainable future [1–3]. For this purpose, photocatalytic conversion of CO₂ into hydrocarbon fuels is becoming a potential solution for eliminating the negative effects of increased CO₂ in the air. In the past 20 years, many kinds of metals (i.e., Ag, Au, Cu, Co, In, etc.) have been loaded on photocatalysts, and their contributions as the active sites of photocatalytic CO₂ reduction (PCR) have been extensively studied [4]. Among them, Cu species exhibited unique properties in converting CO₂ into multi-carbon (C₂₊) products such as ethane, ethanol, and acetic acid (CH₃COOH) [5–9]. Much work has been devoted to improving the design of the photocatalysts and the conversion rate of CO₂, especially to reveal the relationships between the selectivity of the final products and the evolution of Cu species (i.e., valance state and coordination environment) during the reactions.

Recent research demonstrated that Cu^{δ+} (0 < δ < 2) on the surface of catalysts played important roles in C-C coupling in both electrocatalytic

and photocatalytic reduction of CO₂ [10,18,19]. Since the valance state of Cu tends to change, it is critical to determine the valance state of the Cu active sites. Different from the electrocatalytic reduction of CO₂, the photocatalytic reduction of Cu²⁺ to Cu⁺ is less efficient [11]. This implies that the intermediates need a longer time to complete the C-C coupling reaction in PCR. Zhao et al. reported that in the preliminary process of photocatalytic reaction, the pre-activation constructed unique surface active sites on the catalyst: Cu²⁺ on the surface was reduced to Cu⁺ by photogenerated electrons, and these active sites were proved to be used to capture the in situ produced CO and for following C-C coupling reaction [12]. However, if the photocatalytic reaction is carried out in an aqueous environment, the situation becomes different. Cu⁺ is easily disproportionated in an aqueous solution to form stable Cu²⁺ and Cu, which is not able to adsorb CO* intermediate [13]. Previous research on the photocatalytic production of C₂₊ chemicals has emphasized the importance of maintaining the Cu⁺ state during the photocatalysis process. However, it is a very challenging problem to maintain the stability of Cu⁺ in an aqueous solution to improve the

* Corresponding author.

** Corresponding author at: State Key Laboratory of High Performance Ceramics and Superfine Microstructure, Shanghai Institute of Ceramics Chinese Academy of Sciences, Shanghai 200050, China.

E-mail addresses: lingzhang@mail.sic.ac.cn (L. Zhang), wzwang@mail.sic.ac.cn (W. Wang).

<https://doi.org/10.1016/j.apcatb.2022.122177>

Received 4 September 2022; Received in revised form 2 November 2022; Accepted 11 November 2022

Available online 14 November 2022

0926-3373/© 2022 Elsevier B.V. All rights reserved.

lifetime of CO* intermediate to facilitate the conversion of CO₂ to value-added fuels.

Herein, we report a two-dimensional (2D) WO₃ based photocatalyst with single atom Cu/Pt which could selectively convert CO₂ to CH₃COOH with high efficiency. Because of the reductive W⁵⁺ in the 2D WO₃ catalyst, the introduction of Cu²⁺ and Pt⁴⁺ would be partially reduced to Cu⁺ and Pt²⁺, respectively, and multi-coordination complexes with Cl ions formed in the reaction [14,15]. Due to the chemical affinity between Cl and Cu, Cl ions tend to coordinate with Cu species. Cu⁺ forms a complex with Cl in an aqueous solution. The powerful complexing ability of the complexes plays a stabilizing role for Cu⁺ so that CO is activated by the coordination of the complex through the δ-π bond [16,17]. On one hand, single-atom Cu coordinated with Cl is beneficial for the C-C coupling. On the other hand, the transfer of protons from the Pt sites to the CO* intermediate increases the PCR efficiency of producing C₂₊ chemicals. This also confirms the importance of the valence state of the active site and ligand in adsorbing CO and producing C₂₊ chemicals, thus providing a new framework for enhancing PCR activity.

2. Methods

2.1. Materials

All chemicals, cupric chloride (CuCl₂·2H₂O), chloroplatinic acid (H₂PtCl₆), sodium tungstate dihydrate (Na₂WO₄·2H₂O), hydrazine hydrate (N₂H₄·H₂O), hydrochloric acid (HCl), nitric acid (HNO₃), sodium sulfate (Na₂SO₄), phosphoric acid (H₃PO₄), methanol (CH₃OH), ethanol (CH₃CH₂OH), formic acid (HCOOH), acetic acid (CH₃COOH) and sodium chloride (NaCl) were all of the analytical grades and purchased from Sinopharm Chemical Reagent Co., Ltd. All chemicals were used as received after purchase.

2.2. Catalyst preparation

In a typical procedure, 2D WO₃ was prepared by a hydrothermal method [20]. Briefly, Na₂WO₄·2H₂O (1.48 g) was dissolved in deionized water (30 mL), then N₂H₄·H₂O (130 μL) was added to the solution and stirred for 1 h. The mixture was then adjusted to a pH value of 0.55 using HCl (12 mol L⁻¹). After stirring for 10 h, the solution was poured into a 50 mL reaction reactor and kept at 393 K for 12 h. Then the samples were washed several times with deionized water and dried at 333 K for 12 h.

Metal-modified 2D WO₃ was prepared according to a reported paper. 2D WO₃ (0.5 g) was dispersed in water (100 mL). Then appropriate amounts of H₂PtCl₆ and CuCl₂·2H₂O compositions were mixed to form a uniform aqueous solution. The mixture was stirred for 12 h in the dark. The samples were then isolated and freeze-dried. The photocatalysts with theoretical Cu or Pt content of 2.0% were denoted as Cu₂/WO₃ and Pt₂/WO₃, respectively. The photocatalysts with theoretical Cu content of 2.0% and x wt% Pt (x = 1.0, 2.0) was denoted as Cu₂Pt₁/WO₃ and Cu₂Pt₂/WO₃, respectively.

2.3. Characterization

X-ray diffraction (XRD) patterns were obtained on a Rigaku Miniflex II desktop X-ray diffractometer using Cu Kα radiation at a scan speed of 4°/min. The elemental contents of Cu and Pt were determined on an inductively coupled plasma (ICP). Diffuse reflectance spectroscopy (DRS) was measured on a Hitachi U-3010 spectrophotometer, with BaSO₄ as a reference. Raman spectrum was measured by a LabRAM HR EvolutionLab-HRDLS 20. X-ray photoelectron spectroscopy (XPS) test measurements were performed on a Thermo Fisher ESCALAB 250Xi XPS microprobe with Al Kα radiation (1253.6 eV). The XPS spectrum deconvolution was performed by the XPS PEAK 41 program with Lorentzian-Gaussian functions. The C 1 s (284.8 eV) was used as the

reference for the calibration. The morphology of the samples was determined by SEM (Hitachi S-4800). Double spherical aberration-corrected TEM and EDX elemental maps were obtained on the JEM-ARM300F. The electron paramagnetic resonance (EPR) measurement of photocatalyst powder was carried out using an Electron-nuclear double resonance spectrometer (EMXnano, Bruker). *In situ* Fourier transforms infrared (FTIR) spectra were performed on an MCT detector (Nicolet iS10). The X-ray absorption fine structure (XAFS) measurements were carried out at the 1W1B station in Beijing Synchrotron Radiation Facility (BSRF, Beijing). XAFS data reduction and analysis were processed by Athena software in the IFEFFIT software packages. Quantitative chemical configuration analyses of samples were also carried out through the least-squared EXAFS fitting in Artemis software. The CO₂ temperature-programmed experiments (CO₂-TPD) and CO temperature-programmed experiments (CO-TPD) were conducted on an Auto Chem II 2920 instrument. Mass Spectrometry by thermal gravity was performed on an Agilent Gas Chromatography-Mass Spectrometer (7890B-5977B).

2.4. Photocatalytic CO₂ reduction

The reaction was carried out in a 700 mL of glass liquid-solid reactor. 0.04 g catalysts, 15 mmol L⁻¹ HCl, and 20 mL water were mixed. Then, high-purity CO₂ was introduced into the reactor for 30 min. The light source is a 300 W xenon lamp (Perfect Light, PLS-SXE300). The temperature was maintained at 288 K by circulating water. The catalytic reaction lasted for 2 h under the light. The liquid products (HCOOH and CH₃COOH) were analyzed by ion chromatography (Thermo Fisher ICS-6000). CO and CH₄ were analyzed by gas chromatography (GC, Tianmei 7890) equipped with a TDX-01 column and flame ionization detector (FID). CH₃OH and CH₃CH₂OH were analyzed by gas chromatography (GC, Tianmei 7890) equipped with SE-54 column and FID Detection. H₂ and O₂ were analyzed by a gas chromatograph (Tianmei 7890II) equipped with a molecular sieve column (5 A 80/100) and a thermal conductivity detector.

2.5. Photoelectrochemical measurements

The measurements were based on Chenhua CHI 660D electrochemical workstation equipped with A CHF-XM-500 W Xe-lamp. Moreover, a three-electrode system was built using a Pt plate as the counter electrode, an Ag/AgCl electrode as a reference electrode, and an experimental sample as the working electrode. The experimental samples were prepared on FTO conductive glasses (1 cm * 1 cm). The electrolyte was 0.2 M Na₂SO₄ aqueous solution. The photochemical catalyst (1 mg) and Nafion-alcohol solution (10 μL) were mixed, then well-dispersed in ethanol. A thin film of the sample was uniformly deposited on FTO. The working electrode was dried at 80 °C for 24 h. The working electrode was used for further measurements.

3. Results and discussion

3.1. Structure and morphology

Two-dimensional (2D) WO₃ was used as the photocatalyst for the conversion of CO₂, due to its excellent performance in the storage and transfer of electrons and protons [20]. Fig. S1 showed the XRD patterns of the prepared samples, which were indexed as hexagonal cells reported in the literature. After the Cu and Pt species were introduced into 2D WO₃, there was no change in the crystal structure of 2D WO₃, suggesting the high dispersion of Cu and Pt species. The vibration modes of the samples are characterized by Raman spectra, which are shown in Fig. S2. Compared with 2D WO₃, the peaks at 230 cm⁻¹ and 821 cm⁻¹ were shifted slightly after modification, indicating that modification resulted in minor changes in surface W-O-W bond length or bond angles.

Further, XPS analysis was applied to reveal the valence states of the

elements in all samples. As shown in the W 4f XPS spectra of 2D WO₃ (Fig. S3a), the two peaks at 37.7 eV and 35.6 eV were assigned to the W⁶⁺ species. The peaks at 36.8 eV and 34.7 eV corresponded to typical binding energies of low valence W⁵⁺ [21]. Furthermore, the signal at $g = 1.86$ confirmed the existence of W⁵⁺ in the 2D WO₃ (Fig. S4a) [22]. Then, the signal of W⁵⁺ was not detected in the W 4f XPS spectra and EPR spectra of the Cu and Pt species modified WO₃ sample due to the electron transfer of W⁵⁺ (Figs. S3 and S4). Simultaneously, the UV–vis absorption became weaker with the modification of Cu and Pt species in the 400–800 nm region due to the less amount of W⁵⁺ (Fig. S5), which was in accordance with the XPS results. In the Cu 2p XPS spectrum of Cu₂Pt₂/WO₃, the peaks with the binding energy of 935.1 eV and 955.2 eV were attributed to Cu²⁺, while the peaks at 932.6 eV and 952.7 eV were attributed to the Cu⁺ or Cu⁰ (Fig. 1a) [23,24]. Actually, it is difficult to distinguish Cu⁺ and Cu⁰ for Cu XPS due to the overlapping of the peaks. Cu LMM showed a peak at 570 eV, suggesting that Cu⁺ species existed on the surface of Cu₂Pt₂/WO₃ (Fig. 1b). [53] There are two peaks at 73.2 eV and 76.5 eV, which could be attributed to Pt²⁺ (Fig. 1c) [25–27]. The observation suggested that the electron transfer between low valence W and metal-loaded species stabilizes Cu⁺ and Pt²⁺ on 2D WO₃.

To further explore the chemical state of Cu atoms, X-ray Absorption Near Edge Spectroscopy (XANES) was carried out to investigate the electronic structure and bonds of surface atoms in the local environments. Compared with the reference, the absorption edge of Cu in Cu₂Pt₂/WO₃ indicated the valance state of Cu is between 0 and +2 (Fig. 1d), which was consistent with the results from XPS [28]. The Fourier-transformed extended X-ray absorption fine structure (EXAFS) spectra revealed that there was a Cu–O coordination peak at 1.5 Å of the Cu₂Pt₂/WO₃ sample but no Cu–Cu signal was detected (Fig. 1e) [29]. In particular, the peak at about 2.5 Å corresponding to the second coordination shell of Cu–Cu in copper oxides (CuO, Cu₂O) and the peak at about 2.2 Å corresponding to the first coordination shell of Cu–Cu in Cu

metal were not observed, which excluded the presence of Cu nanoparticles or Cu oxides. The detailed information on Cu K-edge EXAFS fitting is listed in Table 1, Figs. 1f and S6. The above results illustrated that the isolated Cu atoms from the Cu₂Pt₂/WO₃ were coordinated to O atoms at an average atom distance of 1.94 Å (Cu–O) and a coordination number of 2.9. Combined with the above HAADF-STEM results, this monatomic dispersion state of Cu could be confirmed.

TEM and SEM images (Fig. S7) demonstrated that WO₃ consisted of two-dimensional sheet structures with a thickness of about 10 nm and sheet sizes between 20 nm and 60 nm. The aberration-corrected high-angle annular dark-field scanning transmission electron microscopy (HAADF-STEM) images confirmed that the regular six-membered channels structure was based on the arrangement of (WO)₆ octahedron, fully exposed on the (001) plane of 2D WO₃ (Figs. 2a and S7d). In further analysis of the channel structure, additional bright spots were observed in some hexagonal channels, which were not found in the unloaded samples. The less bright spots have been clearly distinguished as Cu atoms in the STEM image due to the different atomic numbers of Cu (28th) and W (74th) atoms. Combined with the XANES analysis, single-atom Cu is mainly dispersed inside the WO₃ hexagonal pores, and

Table 1

Structural parameters extracted from the Cu K-edge EXAFS curve-fitting of Cu foil and Cu₂Pt₂/WO₃ samples in Artemis software.

Sample	Bond	N	R (Å)	S ₀ ²	σ ² (10 ^{−3} Å ²)	ΔE ₀ (eV)	R-factor
Cu foil	Cu–Cu	12	2.532 ± 0.004	0.879	8.771 ± 0.4	4.013 ± 0.9	0.00001
Cu ₂ Pt ₂ /WO ₃	Cu–O	2.9	1.936 ± 0.008	0.879	1.430 ± 0.7	−4.114 ± 1.9	0.00007

Note: N is the coordination number; R is interatomic distance; S₀² is the amplitude reduction factor; σ² is the Debye–Waller factor; ΔE₀ is the edge energy shift.

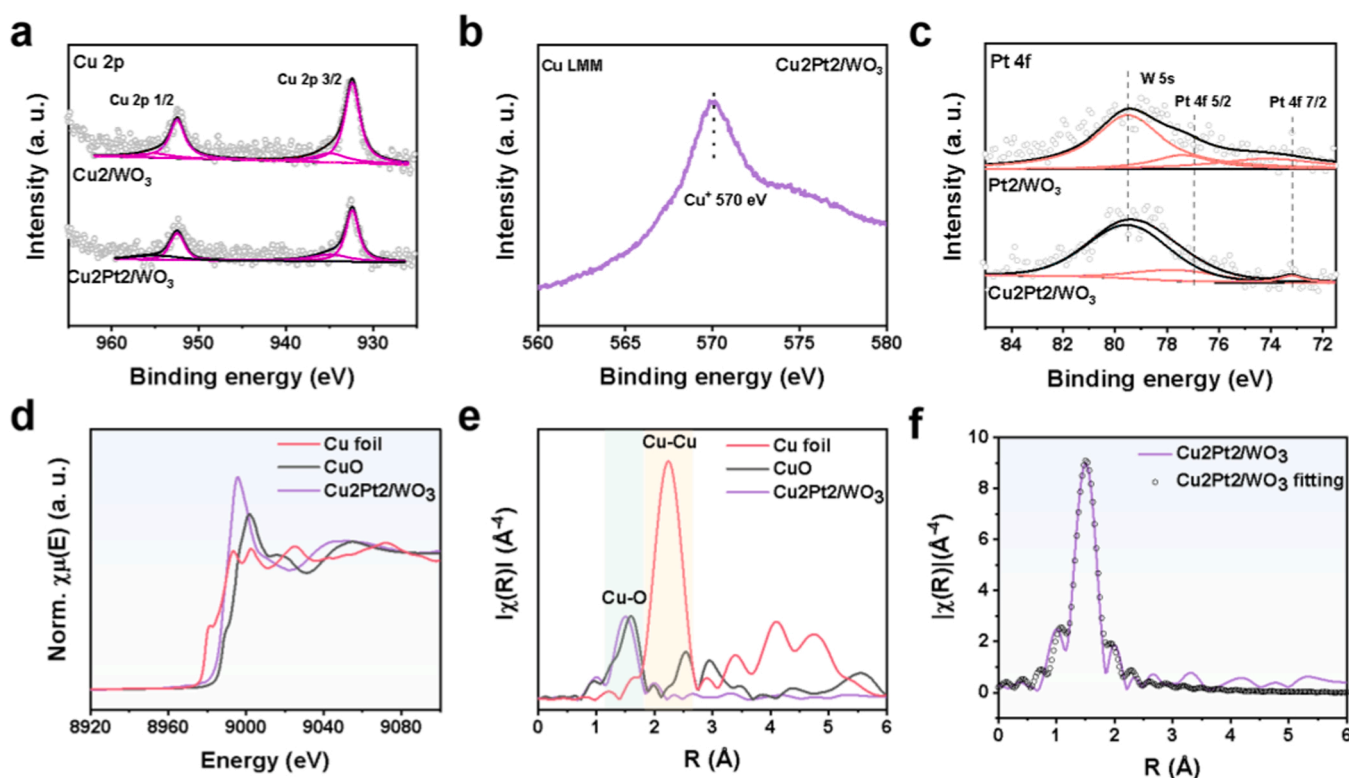


Fig. 1. Characterization of the catalysts. (a) Cu 2p XPS spectra for Cu₂/WO₃ and Cu₂Pt₂/WO₃. (b) Cu LMM AES spectra of Cu₂Pt₂/WO₃. (c) Pt 4f XPS spectra for Pt₂/WO₃ and Cu₂Pt₂/WO₃. (d) Normalized Cu K-edge XANES spectra of Cu foil, CuO, and Cu₂Pt₂/WO₃. (e) XANES spectra at the Cu K-edge of Cu foil, CuO, and Cu₂Pt₂/WO₃. (f) The R-space of Cu K-edge EXAFS for Cu₂Pt₂/WO₃ sample and the corresponding fitting curves.

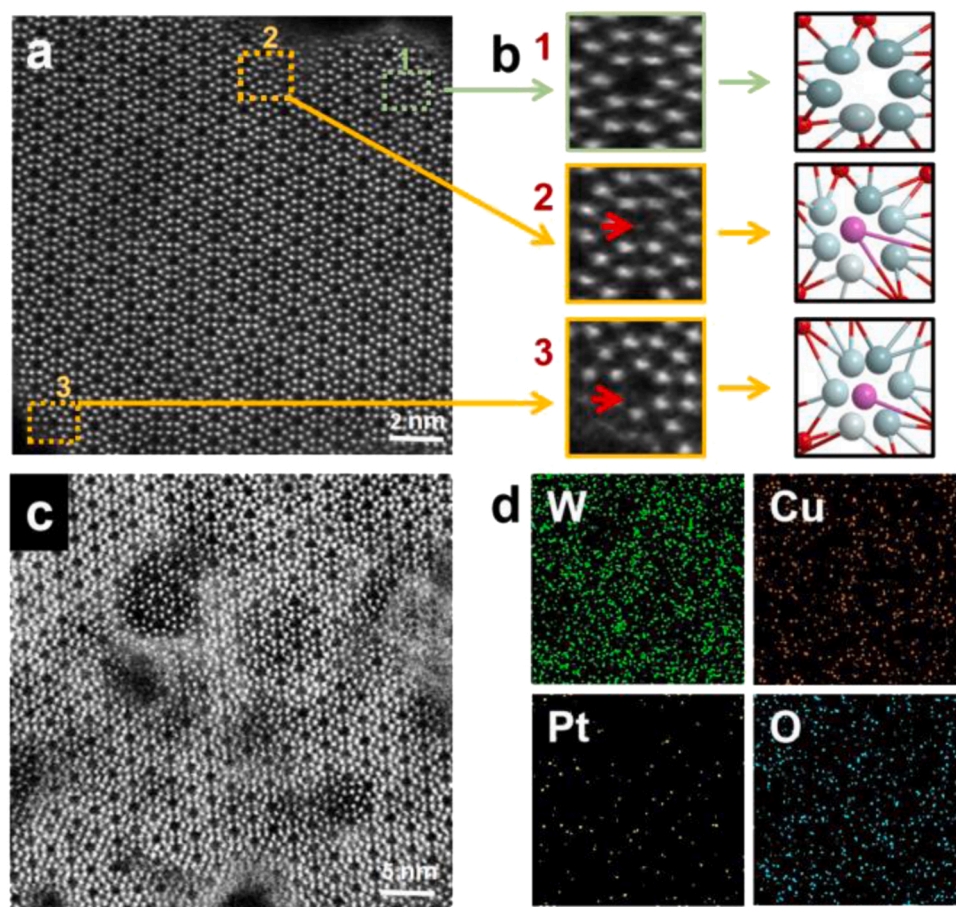


Fig. 2. Structure and morphology characterizations. (a) HAADF-STEM image of the Cu₂Pt₂/WO₃ catalyst. (b) Models of Cu₂Pt₂/WO₃ as referred to in Fig. 2 a. The green part refers to the simple WO₃ hexagonal pores, while the orange box refers to the position where Cu is dispersed in the 2D WO₃ hexagonal pores. (c, d) EDS elemental mapping profiles with W (green), Cu (orange), Pt (yellow), and O (blue) distribution of the Cu₂Pt₂/WO₃ catalyst.

there is no obvious cluster structure aggregation (Figs. 2b, S7e and S7f). Unfortunately, Pt is not found in the STEM images due to its low amount and similar atomic numbers of Pt (78th) and W (74th). Fig. 2c and d are the elemental mapping images (EDS) of W (green dots), Cu (orange dots), Pt (yellow dots), and O (blue dots), showing that Cu and Pt species are evenly distributed throughout the structure.

3.2. Photocatalytic performance

The PCR performance of the modified 2D WO₃ catalysts was evaluated with a 300 W Xe lamp. To suppress the disproportionation reaction of Cu⁺ to Cu²⁺ and Cu⁰ in the aqueous solution, the solution was adjusted with hydrochloric acid before the catalytic reaction. On the basis of the electron structure analysis on the catalysts, the band structure diagram of Cu₂Pt₂/WO₃ was displayed in Fig. S8. The oxidation level of CO₂ to HCOOH or CH₃COOH is above the valence band, which confirms the potential of Cu₂Pt₂/WO₃ as a photocatalyst for PCR. HCOOH and CH₃COOH were the main products in the reaction solution. Besides, trace amounts of CH₄, CH₃OH, H₂O₂, and CO could also be detected (total product < 0.5 μmol g⁻¹) as the products (Figs. S9 and S10). Control experiments indicated that there was no detectable HCOOH and CH₃COOH generation in the dark or the absence of CO₂ and catalyst, indicating that the products originated from PCR (Fig. S11a).

In Fig. 3a, the Cu₂Pt₂/WO₃ exhibited prominent PCR performance, far exceeding that of pure 2D WO₃ and the samples loaded with Pt or Cu alone. The formation rate of CH₃COOH reached 19.41 μmol g⁻¹ h⁻¹, while the formation rate of HCOOH reached 2.62 μmol g⁻¹ h⁻¹ over the Cu₂Pt₂/WO₃. The selectivity of CH₃COOH was 88.1%. Notably, the

evolution rate of CH₃COOH is observed as 6.73, 3.54, and 7.04 μmol g⁻¹ h⁻¹ on Cu₂/WO₃, Pt₂/WO₃, Cu₂Pt₁/WO₃, respectively. In sharp contrast, the evolution rates of CH₃COOH over Cu₂Pt₂/WO₃ were approximately 5 times higher than that of pristine 2D WO₃. Considering that mechanically mixed Cu₂/WO₃ and Pt₂/WO₃ showed poor CH₃COOH yield, the excellent performance of Cu₂Pt₂/WO₃ would be ascribed to the strong synergistic effect between Cu and Pt species (Fig. S10b). Notably, the formation rates of HCOOH and CH₃COOH over the Cu₂Pt₂/WO₃ in the air were about 4.34 and 1.04 μmol h⁻¹ g⁻¹, respectively, much lower than that in the pure CO₂ (Fig. S10a).

In this work, the enhanced conversion of CO₂ to C₂₊ products is closely related not only to the valence state of Cu species but also to the proton and the coordination microenvironment [30–34]. As shown in Fig. 3b, the adjustment of the amount of hydrochloric acid resulted in a variation in the formation rate of C₂₊ products. Compared with pure water, the formation rate of CH₃COOH increased from 2.49 to 19.41 μmol g⁻¹ h⁻¹ after introducing hydrochloric acid. These results clearly verified that the introduction of protons and Cl ions promoted the C-C coupling. To distinguish the influences of the protons and Cl ions, nitric acid and phosphoric acid were also introduced for comparison (Fig. S11c). The formation rate of CH₃COOH was low under nitric acid and phosphoric acid at the same pH value, 2.16 and 1.49 μmol g⁻¹ h⁻¹, respectively. Hence, it is obvious that the excellent performance of C-C coupling would be largely ascribed to the introduction of Cl ions. In addition, when hydrochloric acid was replaced by NaCl as the Cl ions source, the formation rate of CH₃COOH reached 6.38 μmol g⁻¹ h⁻¹ (Fig. S11d). This means that the highly efficient and selective conversion of CO₂ to CH₃COOH has been achieved in the presence of both protons

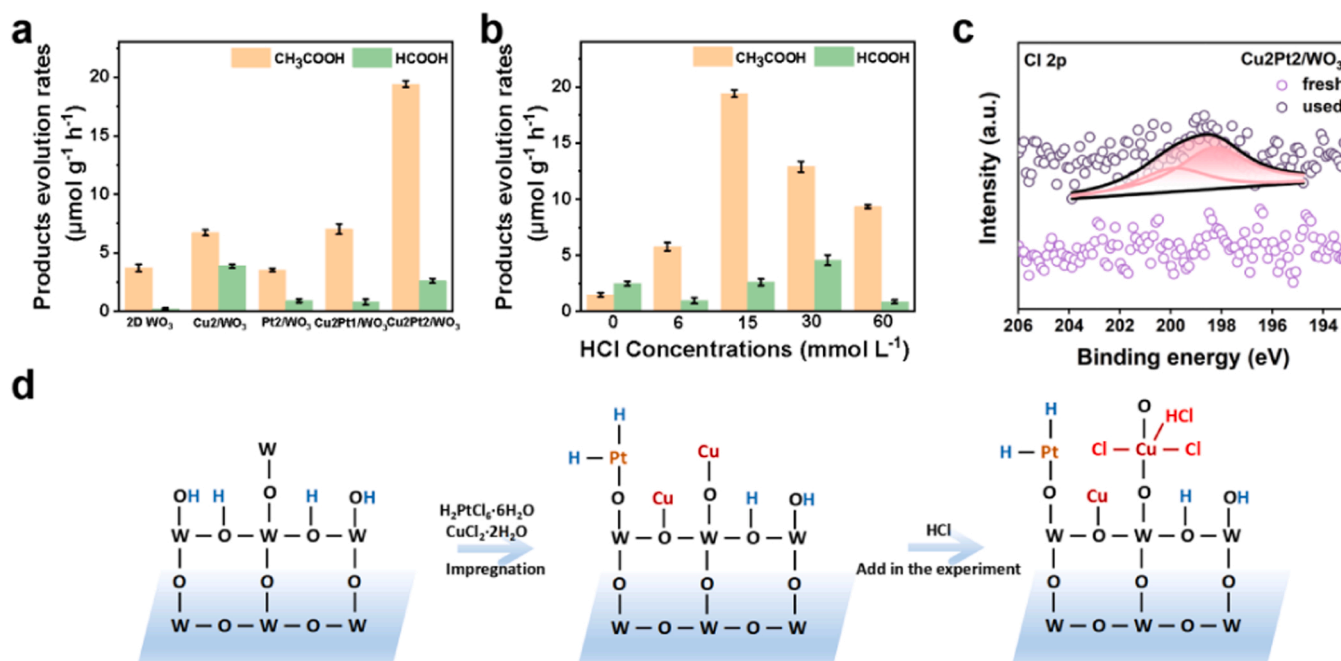


Fig. 3. PCR performance. (a) Photocatalytic activity of 2D WO₃, Cu₂/WO₃, Pt₂/WO₃, Cu₂Pt₁/WO₃, and Cu₂Pt₂/WO₃ catalysts under light irradiation for 2 h. Reaction condition: 288 K, 0.04 g catalysts, 15 mmol L⁻¹ HCl aqueous solution (20 mL), 2 h, 300 W Xe lamp. (b) Photocatalytic activity of Cu₂Pt₂/WO₃ catalysts with different Cl concentrations under light irradiation for 2 h. Reaction condition: 288 K, 0.04 g catalysts, different HCl concentrations aqueous solution (20 mL), 2 h, 300 W Xe lamp. (c) Cl 2p XPS spectrum for the fresh and used Cu₂Pt₂/WO₃. (d) Proposed surface complex formation pathways for metal deposition on the Cu₂Pt₂/WO₃.

and Cl ions.

The enhanced activity and selectivity of PCR performance inspire us to further explore the role of Cl ions. To confirm the existence of Cl ions, XPS and Raman spectroscopy were employed. The Cl 2p XPS spectra for the used Cu₂Pt₂/WO₃ in Fig. 3c showed two peaks at 198.3 eV and 199.9 eV, which could be assigned to the Cu-Cl bond [35]. As revealed by Raman spectra (Fig. S13), the peak at 96 cm⁻¹ is assigned to the Cu-Cl bond in the used Cu₂Pt₂/WO₃ [35]. From the above discussion, it was inferred that the introduction of Cl species would lead to the formation of stable Cu-Cl bonds, which would convert Cu from tetra- to penta- or hexa-coordination (Fig. 3d). The Cl and Pt ions could also form surface complexes with certain coordination numbers [36]. Correspondingly, surface coordination affects the desorption energy of molecules [37,38]. This structure favors the complexation of the CO* intermediate and Cu⁺ through the δ-π coordination bond [39]. The adjacent Pt sites donates protons for the hydrogenation reaction of the CO* intermediate, which accelerates the reduction of CO₂ under visible light irradiation.

The structural stability of catalysts was evaluated. The formation rate of CH₃COOH fluctuated in the cycling tests (Fig. S12). The XRD pattern, EPR spectra, Raman spectra, XPS analysis, and UV-vis absorption spectra of Cu₂Pt₂/WO₃ demonstrated that the phase and the oxidation states were almost identical to that of the pristine sample after the cycling tests (Figs. S13–S16). HAADF-STEM and BF-STEM images (Fig. S17) showed Cu⁺ species remained after the cycle test, further demonstrating Cu and Pt species without extensive exfoliation or aggregation during the PCR process. The yield of CH₃COOH shows a decline after the second cycle, which was mainly caused by covering catalytic active sites. Compared with the FTIR spectrum of fresh samples, characteristic absorption bands of organics were observed at 1320–1583 cm⁻¹, 1636–1792 cm⁻¹ over the used Cu₂Pt₂/WO₃, corresponding to the coordination adsorption of HCOO⁻ and CH₃COO⁻ with Cu or W atoms on the catalyst surface (Fig. S18) [41,42]. The bands at 2850–2997 cm⁻¹ were contributed by the methyl (-CH₃) groups in the CH₃COOH molecules [43,44]. Thermogravimetric analyzer-mass spectrometer (TG-MS) analysis showed that the organics generated in the

reaction were partially adsorbed on the catalyst surface (Fig. S19). However, when the Cu₂Pt₂/WO₃ after the second cycle was re-generated by soaking in aqueous hydrochloric acid, the formation rate of CH₃COOH could be miraculously recovered, reaching 18.4 μmol g⁻¹ h⁻¹ (Fig. S20). These findings demonstrate that the coordination environment between Cl and Cu/Pt species plays an important role in the selectivity control toward CO₂ reduction to solely generate CH₃COOH. Therefore, this optimized catalytic system supplied an ideal platform for studying the effect of CO₂ photocatalytic reactions.

3.3. The functioning mechanism of C-C coupling

As discussed above, C₂+ product production from direct CO₂ conversion involves multi-step complex reaction networks in which the challenging C-C coupling pathway remains difficult to be controlled [40, 46]. To understand the pathway of CO₂ reduction, in situ FTIR spectra were recorded to characterize the reaction intermediates and explore the possible photocatalytic mechanism of C-C coupling (Figs. 4 and S21). For the three samples, no additional peaks appeared before light irradiation except for the distinct linear adsorption of CO₂ at 2292 cm⁻¹ (Fig. 4a) [47]. New peaks appeared with the increase of irradiation time, indicating the presence of different intermediates. The peak at around 1564 cm⁻¹ corresponded to hydrocarboxylate (HCO₃), while the peak in the range of 1400–1590 cm⁻¹ was associated with bidentate (b-CO₃²⁻) or monodentate carbonates (m-CO₃²⁻) (Fig. 4b). Moreover, the peaks at 1605 cm⁻¹ were strengthened with the irradiation time and they were assigned to COOH* intermediates [45,48], which was consistent with the promotion of the CO* formation and the subsequent C-C coupling. Additionally, the peaks at 2105 cm⁻¹ were related to the newly formed adsorbed CO on Cu⁺ (Cu-CO), which is consistent with previous reports (Fig. 4a) [47,48]. The adsorption peaks of CO were weak in those of Cu₂/WO₃ and Pt₂/WO₃ due to the weak adsorption of CO. The peak at 1960 cm⁻¹ was also observed in Cu₂Pt₂/WO₃ and Cu₂/WO₃, which is assignable to the approach of double CO* molecules [50]. Combining the results of the above, the Cu₂Pt₂/WO₃ substantially enhances the

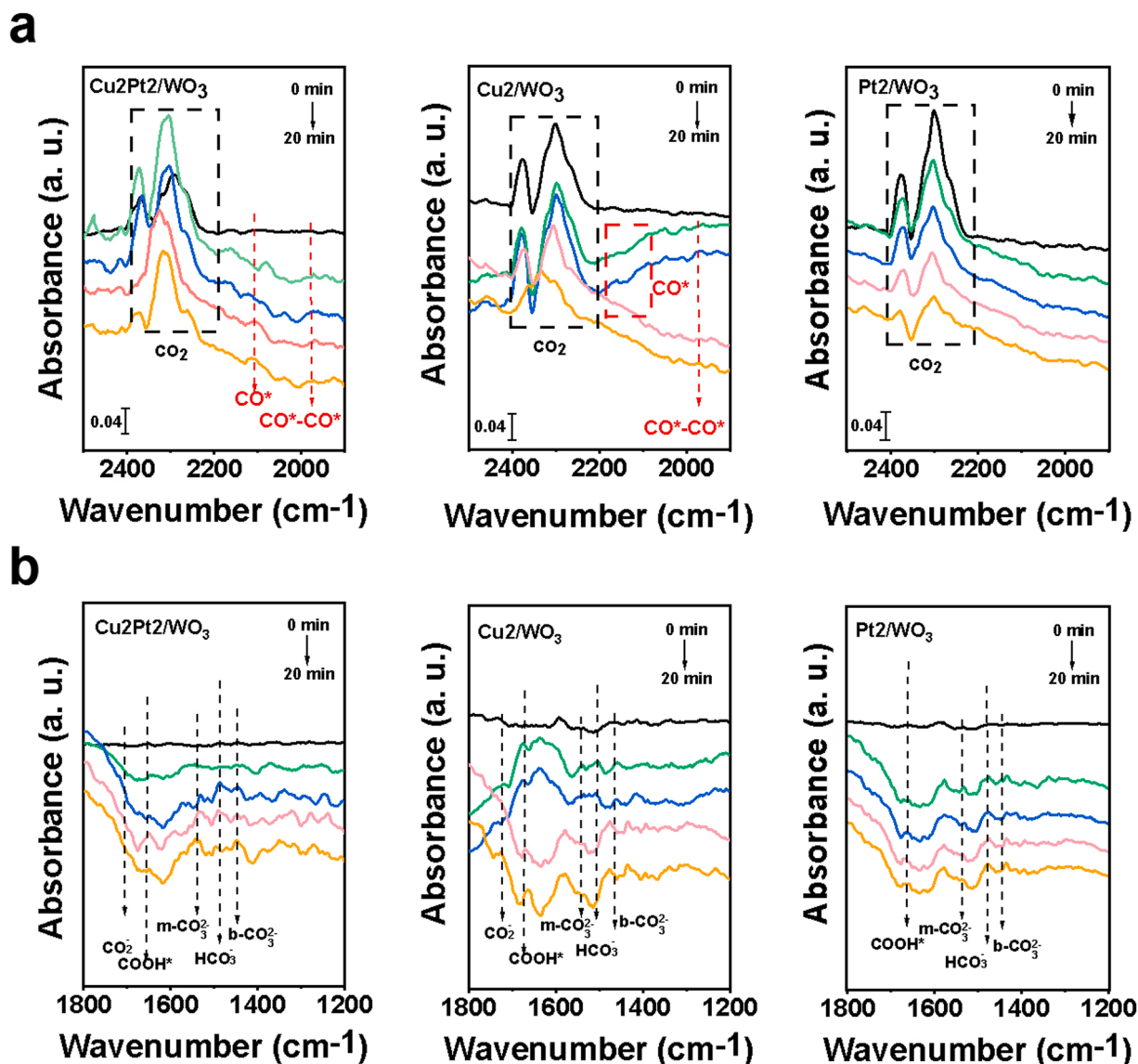


Fig. 4. *In situ* FTIR spectra of different catalysts were collected every 5 min under irradiation in the presence of CO₂ and H₂O in the ranges of (a) 2500–1900 cm⁻¹, and (b) 1800–1200 cm⁻¹, respectively. The spectra collected at 0 min of irradiation in CO₂ and H₂O were used as background.

optimal generation of COOH* and CO* intermediate, and the dimerization of double CO* intermediates, which promotes the C-C coupling process.

As shown in Fig. S21, the photocurrent-time curves of all samples were measured by the photoelectrochemical method [49,51]. Cu₂/WO₃ and Cu₂Pt₂/WO₃ show higher photocurrent intensity than Pt₂/WO₃ and 2D WO₃, indicating that Cu species facilitated the efficient carriers separation. Meanwhile, it was found that Pt modified sample showed less intensive photocurrent than that of the Cu₂/WO₃ sample. It means that Pt species trapped the photoinduced electron, resulting in a less intensive photocurrent. These electrons would transfer to the absorbed CO₂ with protons for improving the PCR efficiency of reductive chemicals. These photoelectrochemical results are in good accordance with the catalytic activity test.

To further investigate the activation and reduction process of CO₂ molecules, CO₂ temperature-programmed desorption (CO₂ TPD) was provided in Fig. S22a [14]. 2D WO₃ exhibited a weak desorption peak at around 357 K whereas Cu₂Pt₂/WO₃ displayed a desorption peak around 490 K. This observation suggested a difference in the CO₂ desorption performance of the catalysts. The result is also verified by CO TPD again, as shown in Fig. S22b [52]. Compared with 2D WO₃, Cu₂/WO₃, and

Pt₂/WO₃, the Cu₂Pt₂/WO₃ exhibited a strong CO desorption peak above 573 K which was assigned to the chemisorbed CO in the form of surface carbonate species, showing relatively strong CO adsorption sites. These observations demonstrated that the introduction of Cu and Pt in Cu₂Pt₂/WO₃ enhanced the surface localized CO concentration and promoted the activity as well as the selectivity for CO₂ reduction.

4. Conclusion

In summary, we designed a 2D WO₃ photocatalyst deposited by single-atom Cu and Pt to trigger the C-C coupling for selective photo-reduction of CO₂ to high value-added CH₃COOH products. The experimental studies revealed the productivity of CH₃COOH over the Cu₂Pt₂/WO₃ catalyst was 19.41 μmol g⁻¹ h⁻¹, which was significantly higher than that of pristine 2D WO₃, Cu₂/WO₃, and Pt₂/WO₃, respectively. The HAADF-STEM images and XANES spectroscopy provided strong evidence that single-atom Cu sites were bonded at the atomic level. Furthermore, the introduction of a small amount of Cl facilitated the formation of coordination structures between Cl ions and Cu or Pt, which enhanced the activity and selectivity of PCR. The coordination of the carboxylic acid produced in the reaction with Cu species would

affect the selectivity of C_{2+} products in cycling experiments. Fortunately, the photocatalyst designed in this work could be regenerated by immersion in a dilute hydrochloric acid solution. This study provides an in-depth understanding of the C-C coupling mechanism. Our findings could also open up new strategies for efficient photocatalytic CO_2 conversion with promising applications in environmental and energy fields.

CRedit authorship contribution statement

Di Zeng: Investigation, Methodology, Validation, Formal analysis, Writing – original draft. **Haipeng Wang:** Methodology, Formal analysis. **Xiaodi Zhu:** Formal analysis. **Heng Cao:** Formal analysis. **Wenjing Wang:** Data curation, Visualization. **Yu Zhang:** Validation. **Juxue Wang:** Data curation, Visualization. **Ling Zhang:** Conceptualization, Supervision, Funding acquisition. **Wenzhong Wang:** Conceptualization, Supervision, Funding acquisition.

Declaration of Competing Interest

The authors declare that they have no known competing financial interests or personal relationships that could have appeared to influence the work reported in this paper.

Data availability

Data will be made available on request.

Acknowledgments

This work was financially supported by the National Natural Science Foundation of China (51972327, 51972325, 52172256, 52002367). The authors would like to thank Ms. Xuechen Liu, Dr. Yuanyi Zhou, Ms. Yaru Zhang, Ms. Qiuqing Du, and Dr. Ruofan Li for their assistance. The authors also thank the solid support from the 1W1B beamline at Beijing Synchrotron Radiation Facility (BSRF, Beijing).

Author contributions

W. W. and L. Z. conceived the idea and supervised the whole project. D. Z. designed and carried out all the experiments. W. H., Z. X., H. C., W. W., Y. Z., and J. W. contributed to the analysis of the mechanism. All the authors contributed to writing the manuscript and approved the final version of the manuscript for submission.

Appendix A. Supplementary material

Supplementary data associated with this article can be found in the online version at [doi:10.1016/j.apcatb.2022.122177](https://doi.org/10.1016/j.apcatb.2022.122177).

References

- V.K. Abdelkader-Fernández, D.M. Fernandes, C. Freire, Carbon-based electrocatalysts for CO_2 electroreduction produced via MOF, biomass, and other precursors carbonization: a review, *J. CO₂ Util.* 42 (2020) 101268–101350, <https://doi.org/10.1016/j.jcou.2020.101350>.
- P. Saha, S. Amanullah, A. Dey, Selectivity in electrochemical CO_2 reduction, *Acc. Chem. Res.* 55 (2022) 134–144, <https://doi.org/10.1021/acs.accounts.1c00678>.
- E. Gong, S. Ali, C.B. Hiragond, H.S. Kim, N.S. Powar, D.Y. Kim, H. Kim, S. In, Solar fuels: research and development strategies to accelerate photocatalytic CO_2 conversion into hydrocarbon fuels, *Energy Environ. Sci.* (2022) 880–937, <https://doi.org/10.1039/D1EE02714J>.
- R. Daiyan, W.H. Saputera, H. Masood, J. Leverett, X. Lu, R. Amal, A disquisition on the active sites of heterogeneous catalysts for electrochemical reduction of CO_2 to value-added chemicals and fuel, *Adv. Energy Mater.* (2020) 1902106–1902142, <https://doi.org/10.1002/aenm.201902106>.
- E. Vahidzadeh, S. Zeng, A.P. Manuel, S. Riddell, P. Kumar, K.M. Alam, K. Shankar, Asymmetric multipole plasmon-mediated catalysis shifts the product selectivity of CO_2 photoreduction toward C_{2+} products, *ACS Appl. Mater. Interfaces* 13 (2021) 7248–7258, <https://doi.org/10.1021/acsami.0c21067>.
- D. Zang, Q. Li, G. Dai, M. Zeng, Y. Huang, Y. Wei, Interface engineering of MoS₂/Cu heterostructures toward highly selective electrochemical reduction of carbon dioxide into acetate, *Appl. Catal. B* 281 (2021) 119426–119439, <https://doi.org/10.1016/j.apcatb.2020.119426>.
- S. Wang, X. Bai, Q. Li, Y. Ouyang, L. Shi, J. Wang, Selective visible-light-driven highly efficient photocatalytic reduction of CO_2 to C_2H_5OH by two-dimensional Cu₂S monolayers, *Nanoscale Horiz.* 6 (2021) 661–668, <https://doi.org/10.1039/D1NH00196E>.
- X. Wu, Y. Li, G. Zhang, H. Chen, J. Li, K. Wang, Y. Pan, Y. Zhao, Y. Sun, Y. Xie, Photocatalytic CO_2 Conversion of Mo_{0.33}WO₃ directly from the air with high selectivity: insight into full spectrum-induced reaction mechanism, *J. Am. Chem. Soc.* 141 (2019) 5267–5274, <https://doi.org/10.1021/jacs.8b12928>.
- B.H. Lee, E. Gong, M. Kim, S. Park, H.R. Kim, E. Jung, C.W. Lee, J. Bok, Y. Jung, Y. S. Kim, K.S. Lee, S.P. Cho, J.W. Jung, C.H. Cho, S. Lebeque, K.T. Nam, H. Kim, S. In, T. Hyeon, Electronic interaction between transition metal single-atoms and anatase TiO₂ boosts CO_2 photoreduction with H₂O, *Energy Environ. Sci.* 15 (2022) 601–609, <https://doi.org/10.1039/D1EE01574E>.
- V.S.S. Mosali, X. Zhang, Y. Liang, L. Li, G. Puxty, M.D. Horne, A. Brajter Toth, A. M. Bond, J. Zhang, CdS-enhanced ethanol selectivity in electrocatalytic CO_2 reduction at sulfide-derived Cu-Cd, *ChemSusChem* 14 (2021) 2924–2934, <https://doi.org/10.1002/cssc.202100903>.
- S. Ali, A. Razzaq, H. Kim, S. In, Activity, selectivity, and stability of earth-abundant CuO/Cu₂O/Cu⁰-based photocatalysts toward CO_2 reduction, *Chem. Eng. J.* 429 (2022) 131579–131602, <https://doi.org/10.1016/j.cej.2021.131579>.
- W. Wang, C. Deng, S. Xie, Y. Li, W. Zhang, H. Sheng, C. Chen, J. Zhao, Photocatalytic C-C coupling from carbon dioxide reduction on copper oxide with mixed-valence copper(I)/copper(II), *J. Am. Chem. Soc.* 143 (2021) 2984–2993, <https://doi.org/10.1021/jacs.1c00206>.
- S.J. Hoseini, R.H. Fath, Formation of nanoneedle Cu(0)/CuS nanohybrid thin film by the disproportionation of a copper(I) complex at an oil-water interface and its application for dye degradation, *RSC Adv.* 6 (2016) 76964–76971, <https://doi.org/10.1039/C6RA14995B>.
- H. Wang, L. Zhang, Y. Zhou, S. Qiao, X. Liu, W. Wang, Photocatalytic CO_2 reduction over platinum modified hexagonal tungsten oxide: effects of platinum on forward and back reactions, *Appl. Catal. B* 263 (2020) 118240–118331, <https://doi.org/10.1016/j.apcatb.2019.118331>.
- Y.F. Li, W. Lu, K. Chen, P. Duchesne, A. Jelle, M. Xia, T.E. Wood, U. Ulmer, G. A. Ozin, Cu Atoms on nanowire Pd/H₂WO_{3-x} bronzes enhance the solar reverse water gas shift reaction, *J. Am. Chem. Soc.* 141 (2019) 14991–14996, <https://doi.org/10.1021/jacs.9b08030>.
- C.T.J. Low, C.P.D. Leon, F.C. Walsh, Copper deposition and dissolution in mixed chloride-sulphate acidic electrolytes: Cyclic voltammetry at static disc electrode, *Trans. Inst. Met. Finish.* 93 (2015) 74–81, <https://doi.org/10.1179/0020296714Z.000000000220>.
- C.H. Gammons, Experimental investigations of the hydrothermal geochemistry of platinum and palladium: IV. The stoichiometry of Pt (IV) and Pd (II) chloride complexes at 100 to 300°C, *Geochim. Cosmochim. Acta* 60 (1996) 1683–1694, [https://doi.org/10.1016/0016-7037\(93\)90409-P](https://doi.org/10.1016/0016-7037(93)90409-P).
- H. Peng, M.T. Tang, J.H. Stenlid, X. Liu, F. Abild-Pedersen, Trends in oxygenate/hydrocarbon selectivity for electrochemical CO_2 reduction to C_2 products, *Nat. Commun.* 13 (2022) 1–11, <https://doi.org/10.1038/s41467-022-29140-8>.
- G.M. Tomboc, S. Choi, T. Kwon, Y.J. Hwang, K. Lee, Potential link between Cu surface and selective CO_2 electroreduction: perspective on future electrocatalyst designs, *Adv. Mater.* 32 (2020) 1908398–1908421, <https://doi.org/10.1002/adma.201908398>.
- J. Besnardiere, B. Ma, A. Torres-Pardo, G. Wallez, H. Kabbour, J.M. González-Calbet, H.J.V. Bardeleben, B. Fleury, V. Buisette, C. Sanchez, T.L. Mercier, S. Cassaignon, D. Portehault, Structure and electrochromism of two-dimensional octahedral molecular sieve h'-WO₃, *Nat. Commun.* 10 (2019) 1–10.
- N. Zhang, A. Jalil, D. Wu, S. Chen, Y. Liu, C. Gao, W. Ye, Z. Qi, H. Ju, C. Wang, X. Wu, L. Song, J. Zhu, Y. Xiong, Refining defect states in W₁₈O₄₉ by mo doping: A strategy for tuning N₂ activation towards solar-driven nitrogen fixation, *J. Am. Chem. Soc.* 140 (2018) 9434–9443, <https://doi.org/10.1021/jacs.8b02076>.
- H. Bruce, Carbonyl chemistry of the group 10 metals, *J. Organomet. Chem.* 44 (1972) 209–227, [https://doi.org/10.1016/S0022-328X\(00\)82907-1](https://doi.org/10.1016/S0022-328X(00)82907-1).
- G. Yanga, P. Qiu, J.Y. Xiong, X.T. Zhua, G. Cheng, Facile anchoring Cu₂O nanoparticles on mesoporous TiO₂ nanorods for enhanced photocatalytic CO_2 reduction through efficient charge transfer, *Chin. Chem. Lett.* 33 (2022) 3709–3712, <https://doi.org/10.1016/j.cclet.2021.10.047>.
- M.E. Aguirre, R. Zhou, A.J. Eugene, M.I. Guzman, M.A. Grela, Cu₂O/TiO₂ heterostructures for CO_2 reduction through a direct Z-scheme: protecting Cu₂O from photo corrosion, *Appl. Catal. B* 217 (2017) 485–493, <https://doi.org/10.1038/s41467-018-07774-x>.
- X.W. Shi, C. Dai, X. Wang, J.Y. Hu, J.Y. Zhang, L.X. Zheng, L. Mao, H.J. Zheng, M. S. Zhu, Protuding Pt single-sites on hexagonal ZnIn₂S₄ to accelerate photocatalytic hydrogen evolution, *Nat. Commun.* 13 (2022) 1287–1297, <https://doi.org/10.1038/s41467-022-28995-1>.
- G.C. Xi, J.H. Ye, Q. Ma, N. Su, H. Bai, C. Wang, In situ growth of metal particles on 3D urchin-like WO₃ nanostructures, *J. Am. Chem. Soc.* 134 (2012) 6508–6511, <https://doi.org/10.1021/ja211638e>.
- W.M. Xie, Z. Huang, R.Q. Wang, C. Wen, Y. Zhou, Metallic Pt and PtO_x dual-cocatalyst-loaded WO₃ for photocatalytic production of peroxydisulfate and hydrogen peroxide, *J. Mater. Sci.* 55 (2020) 11829–11840, <https://doi.org/10.1007/s10853-020-04837-7>.

- [28] D. Grandjean, H.L. Castricum, J.C. Heuvel, B.M. Weckhuysen, Highly mixed phases in ball-milled Cu/ZnO catalysts: an EXAFS and XANES study, *J. Phys. Chem. B* 110 (2006) 16892–16901, <https://doi.org/10.1021/jp055820i>.
- [29] W. Hang, C. Huang, Q. Xiao, L. Yu, L. Shuai, P. An, J. Zhang, M. Qiu, Z. Ren, Y. Yu, Atypical oxygen-bearing copper boosts ethylene selectivity toward electrocatalytic CO₂ reduction, *J. Am. Chem. Soc.* 142 (2020) 11417–11427, <https://doi.org/10.1021/jacs.0c01562>.
- [30] L. Niu, Z. Liu, G. Liu, M. Li, X. Zong, D. Wang, L. An, D. Qu, X. Sun, X. Wang, Z. Sun, Surface hydrophobic modification enhanced catalytic performance of electrochemical nitrogen reduction reaction, *Nano Res.* 392 (2022) 1–8, <https://doi.org/10.1016/j.apsusc.2016.09.093>.
- [31] Y. Zhou, Y. Xiao, J. Zhao, A local proton source from carboxylic acid functionalized metal porphyrins for enhanced electrocatalytic CO₂ reduction, *New J. Chem.* 44 (2020) 16062–16068, <https://doi.org/10.1039/D0NJ02900A>.
- [32] H. Xiao, T. Cheng, W.A. Goddard, R. Sundararaman, Mechanistic explanation of the pH dependence and onset potentials for hydrocarbon products from electrochemical reduction of CO on Cu (111), *J. Am. Chem. Soc.* 138 (2016) 483–486, <https://doi.org/10.1021/jacs.5b11390>.
- [33] O.K. Varghese, M. Paulose, T.J. LaTempa, C.A. Grimes, High-Rate solar photocatalytic conversion of CO₂ and water vapor to hydrocarbon fuels, *Nano Lett.* 9 (2009) 731–737, <https://doi.org/10.1021/nl803258p>.
- [34] H.J. Peng, M.T. Tang, J.H. Stenlid, X. Liu, F.A. Pedersen, Trends in oxygenate/hydrocarbon selectivity for electrochemical CO₂ reduction to C₂ products, *Nat. Commun.* 13 (2022) 1399–1410, <https://doi.org/10.1038/s41467-022-29140-8>.
- [35] C. Zhan, Q. Wang, L. Zhou, X. Han, Y. Wanyan, J. Chen, Y. Zheng, Y. Wang, G. Fu, Z. Xie, Z. Tian, Critical roles of doping Cl on Cu₂O nanocrystals for direct epoxidation of propylene by molecular oxygen, *J. Am. Chem. Soc.* 142 (2020) 14134–14141, <https://doi.org/10.1021/jacs.0c03882>.
- [36] C.C. Hung, C.H. Yeh, C.C. Shih, J.R. Chang, Oxychlorination redispersion of Pt catalysts: surface species and Pt-support interactions characterized by X-Ray absorption and FT-IR spectroscopy, *Catalysts* 9 (2019) 362–377, <https://doi.org/10.3390/catal9040362>.
- [37] P. Ren, M. An, P. Yang, J. Zhang, J. Electroanal, Unveiling the synergistic inhibition of Cl[−] copper plating: pivotal roles of adsorption and desorption, *Chem* 898 (2021) 115624–115632, <https://doi.org/10.1016/j.jelechem.2021.115624>.
- [38] A.B. Mukhopadhyay, C.B. Musgrave, J.F. Sanz, Atomic layer deposition of hafnium oxide from hafnium chloride and water, *J. Am. Chem. Soc.* 130 (2018) 11996–12006, <https://doi.org/10.1021/ja801616u>.
- [39] W. Ma, S. Xie, T. Liu, Q. Fan, J. Ye, F. Sun, Z. Jiang, Q. Zhang, J. Cheng, Y. Wang, Electrocatalytic reduction of CO₂ to ethylene and ethanol through hydrogen-assisted C–C coupling over fluorine-modified copper, *Nat. Catal.* 3 (2020) 478–487, <https://doi.org/10.1038/s41929-020-0450-0>.
- [40] S. Zhu, X. Li, X. Jiao, W. Shao, L. Li, X. Zu, J. Hu, J. Zhu, W. Yan, C. Wang, Y. Sun, Y. Xie, Selective CO₂ photoreduction into C₂ product enabled by Charge-Polarized metal pair sites, *Nano Lett.* 21 (2021) 2324–2331, <https://doi.org/10.1021/acs.nanolett.1c00383>.
- [41] X. Qiu, H. Zhu, J. Huang, P. Liao, X. Chen, Highly selective CO₂ electroreduction to C₂H₄ using a metal-organic framework with dual active sites, *J. Am. Chem. Soc.* 143 (2021) 7242–7246, <https://doi.org/10.1021/jacs.1c01466>.
- [42] C. Emmeluth, M.A.A. Suhm, A chemical approach towards the spectroscopy of carboxylic acid dimer isomerism, *Phys. Chem. Chem. Phys.* 5 (2003) 3094, <https://doi.org/10.1039/B303816E>.
- [43] J. Albero, Y. Peng, H. García, Photocatalytic CO₂ reduction to C₂₊ products, *ACS Catal.* 10 (2020) 5734–5749, <https://doi.org/10.1021/acscatal.0c00478>.
- [44] H. Park, H. Ou, A.J. Colussi, M.R. Hoffmann, Artificial photosynthesis of C₁–C₃ hydrocarbons from water and CO₂ on titanate nanotubes decorated with nanoparticle elemental copper and CdS quantum dots, *Phys. Chem. A* 119 (2015) 4658–4666, <https://doi.org/10.1021/jp511329d>.
- [45] T. Zhang, H. Shang, B. Zhang, D. Yan, X. Xiang, Ag/ultrathin-layered double hydroxide nanosheets induced by a self-redox strategy for highly selective CO₂ reduction, *ACS Appl. Mater. Interfaces* 13 (2021) 16536–16544, <https://doi.org/10.1021/acsami.1c02737>.
- [46] J. Zhu, W. Shao, X. Li, X. Jiao, J. Zhu, Y. Sun, Y. Xie, Asymmetric triple-atom sites confined in ternary oxide enabling selective CO₂ photothermal reduction to acetate, *J. Am. Chem. Soc.* 143 (2021) 18233–18241, <https://doi.org/10.1021/jacs.1c08033>.
- [47] A. Wuttig, C. Liu, Q.L. Peng, M. Yaguchi, C.H. Hendon, K. Motobayashi, S. Ye, M. Osawa, Y. Surendranath, Tracking a common surface-bound intermediate during CO₂-to-fuels catalysis, *ACS Cent. Sci.* 2 (2016) 522–528, <https://doi.org/10.1021/acscentsci.6b00155>.
- [48] R.A. Hadden, B. Sakakini, J. Tabatabaei, K.C. Waugh, Adsorption and reaction induced morphological changes of the copper surface of a methanol synthesis catalyst, *Catal. Lett.* 44 (1997) 145–151, <https://doi.org/10.1023/A:1018962016811>.
- [49] M. Tayyab, Y.J. Liu, S.X. Min, R.M. Irfan, Q.H. Zhu, L. Zhou, J.Y. Lei, J.L. Zhang, Simultaneous hydrogen production with the selective oxidation of benzyl alcohol to benzaldehyde by a noble-metal-free photocatalyst VC/CdS nanowires, *Chin. J. Catal.* 43 (2022) 1165–1175, [https://doi.org/10.1016/S1872-2067\(21\)63997-9](https://doi.org/10.1016/S1872-2067(21)63997-9).
- [50] G. Iijima, T. Inomata, H. Yamaguchi, M. Ito, H. Masuda, Role of a hydroxide layer on Cu electrodes in electrochemical CO₂ reduction, *ACS Catal.* 9 (2019) 6305–6319, <https://doi.org/10.1021/acscatal.9b00896>.
- [51] Y.J. Liu, Q.H. Zhu, M. Tayyab, L. Zhou, J.Y. Lei, J.L. Zhang, Single-atom Pt loaded zinc vacancies ZnO–ZnS induced type-V electron transport for efficiency photocatalytic H₂ evolution, *Sol. RRL* 5 (2021) 2100536–2100557, <https://doi.org/10.1002/adma.201505281>.
- [52] Y.N. Chen, D.S. Liu, L.J. Yang, M. Meng, J. Zhang, L.R. Zheng, S.Q. Chu, T.D. Hu, Ternary composite oxide catalysts CuO/Co₃O₄–CeO₂ with wide temperature-window for the preferential oxidation of CO in H₂-rich stream, *Chem. Eng. J.* 234 (2013) 88–98, <https://doi.org/10.1016/j.cej.2013.08.063>.
- [53] I. Platzman, R. Brenner, H. Haick, R. Tannenbaum, Oxidation of Polycrystalline Copper Thin Films at Ambient Conditions, *J. Phys. Chem. C* 112 (4) (2008) 1101–1108, <https://doi.org/10.1021/jp076981k>.